



Laboratory Study of Rate Coefficients for $\text{H}_2\text{:H}_2$ Inelastic Collisions between 295 and 20 K

S. Montero , G. Tejeda , and J. M. Fernández

Laboratory of Molecular Fluid Dynamics, Instituto de Estructura de la Materia, CSIC Serrano 121, E-28006 Madrid, Spain; emsalvador@iem.cfmac.csic.es
Received 2019 August 5; revised 2019 November 7; accepted 2019 November 26; published 2020 February 20

Abstract

A laboratory study of state-to-state rate coefficients (STS rates) for $\text{H}_2\text{:H}_2$ inelastic collisions in the $v = 0$ state is reported. The study, which spans the 295–20 K thermal range, is based on the use of a kinetic master equation. It describes the time-space evolution of populations of H_2 rotational levels as induced by inelastic collisions. It is applied here to a supersonic jet of natural H_2 . This medium bears a large amount of relevant data that allows for the establishment of best values and confidence margins for the dominant STS rates of $\text{H}_2\text{:H}_2$ inelastic collisions on an experimental basis. The primary experimental data derived from the supersonic jet are the local number density, the populations of the H_2 rotational levels, and their gradients along the jet by means of high-sensitivity Raman spectroscopy with superb space resolution. First, two sets of theoretical STS rates from the literature have been tested against the experiment. The set that shows a better agreement with the experiment has then been scaled to derive an improved set of experiment-scaled STS rates (ES rates). They allow the reproduction of more than 50 experimental population gradient data within a standard deviation $< 1.4\%$ along the 295–20 K thermal range. The estimated uncertainty for the ES rates ranges from $\approx 3\%$ near 300 K to $\approx 6\%$ near 20 K. ES rates and uncertainties for $\text{H}_2\text{:H}_2$ ground-state inelastic collisions between 300 and 20 K are presented in machine-readable format. Other (incomplete) sets of theoretical rates from the literature are discussed.

Unified Astronomy Thesaurus concepts: [Astronomy databases \(83\)](#); [Laboratory astrophysics \(2004\)](#); [Molecular spectroscopy \(2095\)](#); [Collision processes \(2065\)](#)

Supporting material: machine-readable table, tar.gz file

1. Introduction

Molecular hydrogen (H_2) is a fundamental ingredient of the universe. It was the first neutral molecular species formed and is the most abundant one. Since the 1970s, it has been detected in a great number of astronomical observations by means of UV and IR spectroscopy. It appears everywhere in many different environments: molecular clouds, planetary nebulae, Herbig–Haro objects, supernova remnants, the Galactic center, the Small Magellanic Clouds, Seyfert galaxies, and interacting galaxies (Sternberg & Dalgarno 1989; Habart et al. 2005). Spectral line intensities of H_2 bear substantial information about the excitation/de-excitation processes, where it acts as an efficient coolant agent. Also the ratio of ortho- H_2 ($o\text{H}_2$) to para- H_2 ($p\text{H}_2$) serves as a probe of the background radiation field (Dalgarno 2000).

Modeling of astronomical media rests on the balance and formation-destruction equations. Fundamental ingredients of those equations are the radiation field intensity and the temperature-dependent rate coefficients for $\text{H}_2\text{:H}_2$ inelastic collisions (Sternberg & Dalgarno 1989). The $\text{H}_2\text{:H}_2$ inelastic collisions have attracted the attention of scientists for more than half a century, and progress in the study of H_2 in astrophysical environments has emphasized the important role of $\text{H}_2\text{:H}_2$ inelastic collision rates. These quantities are difficult to calculate with accuracy and are still more elusive from the experimental point of view.

From the theoretical point of view, $\text{H}_2\text{--H}_2$ is the simplest and more affordable tetraatomic system for developing and testing intermolecular potential energy surfaces (PESs) and advanced quantum scattering methods. The literature is rich in such results. After so much work, one could think that the $\text{H}_2\text{--H}_2$ PES has been definitively established with sufficient accuracy.

However, to date this is not the case. While some rigid-rotor PESs appear to be reasonably good, they are limited to the vibrational ground state. Conversely, full-dimensional PESs that allow describing vibrational excited states are far less accurate for the ground state. A possible reason is the extremely small anisotropic component of the $\text{H}_2\text{--H}_2$ PES, which is difficult to calculate accurately. In fact, it is so small that the H_2 molecules display nearly free rotation in liquid and solid H_2 (Kühnel et al. 2011). Nonetheless, the consequence of such a small anisotropy is of great physical significance, as this is the ultimate reason for the large breakdown of equilibrium between the rotational and translational degrees of freedom in H_2 rarefied media. Such nonequilibrium is by far the largest among all molecular species and represents a serious challenge for the interpretation of gas dynamics in rarefied H_2 media, and in particular of the H_2 -rich regions in space. There the energy balance is controlled by $\text{H}_2\text{:H}_2$ inelastic collisions, together with $\text{H}_2\text{:H}$, $\text{H}_2\text{:H}^+$, and $\text{H}_2\text{:e}^-$ collisions, in interplay with quadrupole radiation emission and absorption. Modeling of such media requires accurate state-to-state rates (STS rates, in short) for the dominant $\text{H}_2\text{:H}_2$ inelastic collision processes. Tangible examples of such equilibrium breakdown are provided in the present work, which is based on a rigorous interpretation of H_2 rarefied media produced in the laboratory.

From the pioneer works on inelastic $\text{H}_2\text{:H}_2$ collisions (Takayanagi 1959, 1965; Arthurs & Dalgarno 1960; Davison 1962; Roberts 1963; Zarur & Rabitz 1974; Green 1975; Rabitz & Lam 1975; Green et al. 1978), quantum scattering methods based on the stationary Schrödinger equation (Köhler & Schaefer 1983; Hutson & Green 1994; Flower et al. 2000; Krems 2006; Lee et al. 2006), on the time-dependent Schrödinger equation (Lin & Guo 2002; Gatti et al. 2005; Otto et al. 2008), or on mixed

quantum/classic theory (Semenov & Babikov 2016) appear to be well established. The calculation of the STS cross sections and rates for $\text{H}_2\text{:H}_2$ collisions seems to be accurate from the theoretical and computational points of view, but the bottleneck for such calculations is the $\text{H}_2\text{-H}_2$ PES. In addition, systematic comparison with experiment is still missing in spite of some preliminary efforts: Audibert et al. (1974, 1975) for the vibrational relaxation, and Maté et al. (2005), Montero et al. (2006), Montero & Pérez-Ríos (2014), and Anikin (2017) for the rotational relaxation within the ground state.

Concerning the present work, several more or less complete sets of STS rates for $\text{H}_2\text{:H}_2$ inelastic collisions in the vibrational ground state based on rigid-rotor PESs have been reported. In a chronological order these sets are as follows:

1. **MS80** rates by Monchick & Schaefer (1980) based on the so-called V_{III} vibrotor **MS80**-PES (W. Meyer & J. Schaefer 1980, unpublished).
2. **D87** rates by Danby et al. (1987) based on **MSL80**-PES (W. Meyer et al. 1980, unpublished), which is an improved version of **MS80**-PES.
3. **F98** rates by Flower (1998) based on **Sw88**-PES (Schwenke 1988).
4. **M06** rates by Montero et al. (2006) based on **DJ00**-PES (Diep & Johnson 2000).
5. **S06** rates by Sultanov & Guster (2006) based on **DJ00**-PES.
6. **L08** rates by Lee et al. (2008) based on **DJ00**-PES.
7. **M14** rates by Montero & Pérez-Ríos (2014) based on **DJ00**-PES.
8. **W18** rates by Wan et al. (2018) based on **P08**-PES (Patkowski et al. 2008).

Among these sets the **M14** rates will be employed in the present work as a scaling reference.

Other rigid-rotor PESs by Schaefer & Köhler (1989), its improved version by Schaefer (1994), and those of Wind & Roegen (1992) have not been employed for the calculation of $\text{H}_2\text{:H}_2$ STS rates as far as we are aware. Calculations based on full-dimensional PESs for $\text{H}_2\text{-H}_2$ interaction have been reported, namely:

1. **L02** rates by Lin & Guo (2002) based on **B02**-PES (Boothroyd et al. 2002) and **ASP94**-PES (Aguado et al. 1994).
2. **O08** rates by Otto et al. (2008) based on **B02**-PES.
3. **B11a** and **B11b** rates by Balakrishnan et al. (2011) based on **B02**- and **H08**-PES (Hinde 2008), respectively.

Collisions involving excited vibrational states of H_2 have also been considered (Flower 2000; Panda et al. 2007; Quemener & Balakrishnan 2009; Balakrishnan et al. 2011; Fonseca dos Santos et al. 2011, 2013; Bohr et al. 2014) employing **Sw88**-PES, **B02**-PES, and/or **H08**-PES. For the vibrational ground state of H_2 the results are, however, worse than those from the rigid-rotor PESs.

In contrast with theory, few experiments capable of providing information on the STS rates for $\text{H}_2\text{:H}_2$ inelastic collisions in the vibrational ground state have been reported. Acoustic ultrasonic absorption experiments on H_2 did provide a few rotational cross sections and/or relaxation-time data (Hermans et al. 1983 and references therein). For pH_2 five data at 293, 170, 111.5, 90.5, and 77.3 K were reported, and for nH_2 , only two, at 293 and 77.3 K.

These data are expressible as a function of generalized cross sections (Schaefer 2010), or of the enough complete set of **M14** rates (Montero & Pérez-Ríos 2014), providing a limited validation for the **M06**, **S06**, **L08**, and **M14** rates above 77 K. A summary of these results has been reported by Montero & Pérez-Ríos (2014). A recent work provides an additional semiquantitative validation (Anikin 2017).

Broadening and shifting of rotational Raman spectral lines of H_2 can, in principle, provide information on the STS rates. However, no results for low-temperature H_2 are known to us, and those at room temperature and above have been inconclusive (Rahn et al. 1991; Le Flohic et al. 1994). A different experimental approach based on the use of supersonic jets was proposed more recently, providing a preliminary validation for the two dominant STS rates involved in $\text{pH}_2\text{:pH}_2$ collisions below 110 K (Maté et al. 2005). A validation extended to $\text{pH}_2\text{:oH}_2$ and $\text{oH}_2\text{:oH}_2$ collisions was reported by Montero et al. (2006). Though these results did provide approximate validations, they require a revision based on the new and far more accurate experimental data reported in the present work. The methodology was then at the developmental stage. It has since been improved substantially in the light of the study of $\text{O}_2\text{:O}_2$ collisions (Pérez-Ríos et al. 2011) and $\text{H}_2\text{O:He}$ collisions (Tejeda et al. 2015).

The present work is based on the above-mentioned supersonic jet methodology. Its first goal is aimed at establishing the dominant STS rates for $\text{pH}_2\text{:pH}_2$, $\text{pH}_2\text{:oH}_2$, and $\text{oH}_2\text{:oH}_2$ inelastic collisions in the vibrational ground state below 300 K on an experimental basis, together with their uncertainties. We employ for this purpose an upgraded version of the underlying theory, as well as a set of high-precision experimental data from several similar nH_2 supersonic jets generated ad hoc for the present purpose at the Laboratory of Molecular Fluid Dynamics (CSIC, Madrid). Experimental details are given in the Appendix. In a first step we assess the STS rates from Montero et al. (2006) and Montero & Pérez-Ríos (2014), and then we scale this latter set to the experiment in order to obtain a high-quality set of STS rates.

As a by-product of the present study, other useful results for a detailed insight into the thermal nonequilibrium problem of H_2 rarefied media have been obtained. Owing to its potential interest, they are included as Supplemental Material in a .tar.gz package and also at doi:10.20350/digitalCSIC/9015.

This paper is structured as follows. In Section 2 the theoretical basis of the renewed methodology is presented. Section 3 includes the discussion of results, with Section 3.1 describing the assessment of previous theoretical STS rates. Section 3.2 describes the improvement of STS rates by a scaling-to-the-experiment procedure. This material, which is the core of the present work, spans the 300–20 K range and is reported in machine-readable form. In Section 3.3 results from the literature are compared with the present experiment-scaled STS rates. Section 4 closes the paper with remarks and conclusions. The Appendix accounts for the experimental details and related procedure. Supplemental Material useful for the discussion of results and interpretation of nonequilibrium behavior in H_2 rarefied media is included in a .tar.gz package and available at doi:10.20350/digitalCSIC/9015.

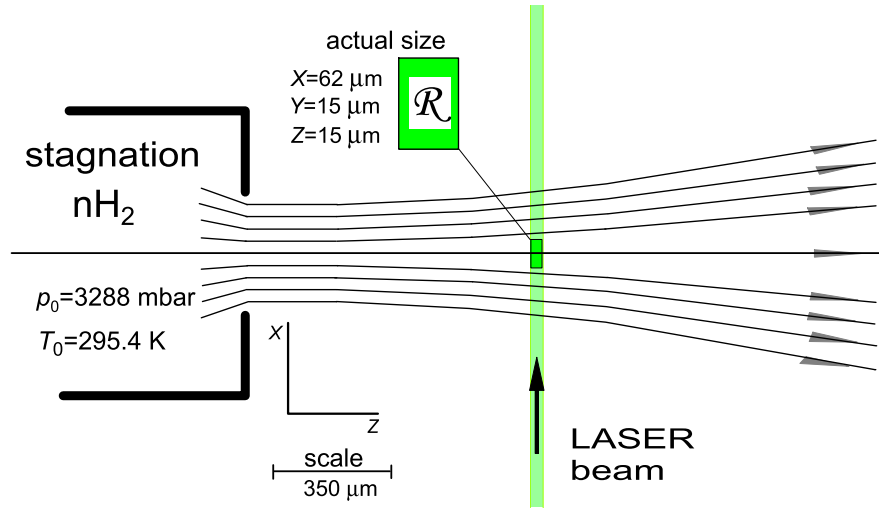


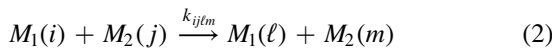
Figure 1. Scheme of nozzle, supersonic jet flow field, and Raman scattering excitation (along X)-collection (along Y) conditions for probe volume \mathcal{R} .

2. Methodology

This work relies on a kinetic master equation (MEQ) that derives from the generalized Boltzmann equation for molecular species, as has been proved by Snider (1998). The generic form of this MEQ reads as

$$\frac{dP_i}{dt} = n \sum_{j,\ell,m} (-P_i P_j k_{ij\ell m} + P_\ell P_m k_{\ell m i j}). \quad (1)$$

It describes the local time evolution of the population probability $P_i(z, t)$ (in short, population) of molecules in a rotational energy level with quantum number $J = i$ as a consequence of inelastic collisions in a gas of distinguishable molecules at local instantaneous number density $n(z, t)$ and translational temperature $T(z, t)$. The $k_{ij\ell m}$ are the temperature-dependent STS rates accounting for the elementary collision process



of a molecule M_1 in the rotational state $J = i$ with another molecule M_2 in the rotational state $J = j$, in a medium at translational temperature T . As a consequence of the collision, the post-collision states of the two molecules become $J = \ell$ and $J = m$. For convenience the first two subscripts will refer from now on to the pre-collision rotational quantum states of the colliding partners, and the last two to the post-collision states.

The STS rates obey the detailed balance relation

$$k_{\ell m i j} = k_{ij\ell m} \frac{(2i+1)(2j+1)}{(2\ell+1)(2m+1)} \times e^{(\epsilon_\ell + \epsilon_m - \epsilon_i - \epsilon_j)/T}, \quad (3)$$

where $\epsilon_i, \epsilon_j, \epsilon_\ell, \epsilon_m$ are the energies of the rotational levels (in kelvin).

The experimental medium considered here is the paraxial region of a steady $n\text{H}_2$ supersonic jet. Its flow field, which is stable for hours, is strictly laminar between nozzle exit and the normal shock formed several nozzle diameters downstream in the expansion. Details about the supersonic jet can be seen in Figure 1 and in Appendix A.1. In the paraxial region of the jet

the spacetime relation is fixed by the local flow velocity

$$v(z) = (dz/dt)_z. \quad (4)$$

This quantity is inferred from the experimental data with very good accuracy. MEQ (1) can be transformed by means of Equation (4) from the time domain into the space domain, which is directly accessible in the experiment. MEQ (1) becomes in this way

$$\frac{dP_i}{dz} = \frac{n}{v} \sum_{j,\ell,m} (-P_i P_j k_{ij\ell m} + P_\ell P_m k_{\ell m i j}), \quad (5)$$

where the flow quantities n, v, P_i and the gradients dP_i/dz only depend on the distance z along the jet and are locally independent of time by virtue of the long-term (hours) stability of the flow field; n, v, P_i , and dP_i/dz in MEQ (5) are obtained experimentally along the jet by means of Raman spectroscopic measurements. Details are given in Appendix A.2. In this way only the STS rates remain in MEQ (5) as unknowns.

For convenience, the rotational quantum numbers $J = 0, 2, 4$ for pH_2 and $J = 1, 3$ for oH_2 are used as i, j, ℓ, m subscripts in MEQ (5). Higher rotational states are not significantly populated in the $T \leq 300$ K range of temperatures of the present work and will be ignored.

Since STS rates for excitation (“up”) and de-excitation (“down”) processes in low-temperature H_2 may differ by many orders of magnitude, it is convenient to reformulate MEQ (5) in terms of only “down” rates, which show a far smoother dependence on T . This simplification is based on the detailed balance relation (3). Moreover, for consistency with symmetry requirements in quantum theory of molecular scattering of H_2 (Maté et al. 2005; Montero et al. 2006), indistinguishable molecules will be considered for $\text{pH}_2\text{:pH}_2$ and $\text{oH}_2\text{:oH}_2$ collisions, and distinguishable molecules for $\text{oH}_2\text{:pH}_2$ collisions. Under these conditions, MEQ (5) can be reduced to the form

$$dP_J/dz = \frac{n}{v} \sum_{turs}^* S_{Jturs} b_{turs} k_{turs}^{\text{down}}, \quad (6)$$

where the constraint $(\epsilon_t + \epsilon_u) > (\epsilon_r + \epsilon_s)$ holds, i.e., in terms of only “down” STS rates, k_{turs}^{down} . Subscripts t, u, r , and s run over the values of the rotational quantum number J allowed by

ortho-para nonconversion. The asterisk in the sum indicates restriction to only one rate representing the several allowed subscript permutations in k_{turs}^{down} . The factorized form of MEQ (6) has important advantages over MEQ (5). Among others, it avoids the repetition of STS rates in MEQ (6) with respect to MEQ (5). It also allows for a deeper insight in the thermal nonequilibrium features of supersonic flow.

The factor

$$S_{Jturs} = -\delta_{Jt} - \delta_{Ju} + \delta_{Jr} + \delta_{Js} \quad (7)$$

defines the sign, + (population) or - (depletion), with which $tu \rightarrow rs$ (de-excitation) and $rs \rightarrow tu$ (excitation) collision processes contribute altogether to the global population evolution of a particular rotational level J . $S_{Jturs} = 0$ indicates that $tu \rightarrow rs$ and $rs \rightarrow tu$ do not modify the population of level J . This S_{Jturs} factor accounts for the conservation of the total probability $\sum_J P_J = 1$ along the collision-induced transfer of population between rotational levels. Hence, the $\sum_J P_J = 1$ conservation condition implies the constraint $\sum_J dP_J/dz = 0$. Therefore, the net result of $tu \rightarrow rs$ and $rs \rightarrow tu$ collisions is additive (+) in some levels and subtractive (-) in others, as shown in Tables S2, S3, and S4 provided in the Supplemental Material in doi:10.20350/digitalCSIC/9015 and in the .tar.gz package.

It can be shown that the b_{turs} factor in MEQ (6) has the form

$$b_{turs} = P_t P_u (1 - e^{-U_{turs}}). \quad (8)$$

It describes the thermal contribution of the bath to the dP_J/dz gradient of a particular rotational level J due to the internal and translational degrees of freedom. Along the jet, prior to the formation of a shock wave, b_{turs} is always positive since U_{turs} , defined as

$$U_{turs} = \epsilon_t Y_t + \epsilon_u Y_u - \epsilon_r Y_r - \epsilon_s Y_s, \quad (9)$$

is also positive for the “down” condition $(\epsilon_t + \epsilon_u) > (\epsilon_r + \epsilon_s)$; ϵ_J are the energies of the rotational levels of H_2 referred to their ground levels ($J=0$ for pH_2 , and $J=1$ for oH_2) expressed in kelvin; $\epsilon_0 = 0$, $\epsilon_1 = 0$, $\epsilon_2 = 509.88$ K, $\epsilon_3 = 844.70$ K, and $\epsilon_4 = 1681.70$ K, (1 K = 0.69502 cm $^{-1}$). In Equation (9) $Y_0 = Y_1 = 0$ holds by definition, while Y_J is defined for $J \geq 2$ as

$$Y_J = \frac{T_{Jg} - T}{T_{Jg} T}. \quad (10)$$

Y_J accounts for the nonequilibrium between the translational and rotational degrees of freedom in the H_2 medium, where T is the (bath) translational temperature; T_{Jg} is the pairwise rotational temperature of level J referred to its ground level g . These experimental rotational temperatures are unambiguously defined by the relation

$$T_{Jg} = \epsilon_J / \ln \left(\frac{(2J+1)P_g}{(2g+1)P_J} \right), \quad (11)$$

where $g=0$ and $g=1$ refer to the rotational ground states of pH_2 and oH_2 species, respectively.

In order to facilitate the interpretation of some physical facts of the collisional problem along the jet (see the files in doi:10.20350/digitalCSIC/9015 and in the .tar.gz package of

Supplemental Material), it is useful to split the b_{turs} factor as

$$b_{turs} = b_{tu} + b_{rs}, \quad (12)$$

with

$$b_{tu} = P_t P_u, \quad \text{and} \quad b_{rs} = -P_t P_u e^{-U_{turs}}. \quad (13)$$

Each $S_{Jturs} b_{turs} k_{turs}^{\text{down}}$ product in MEQ (6) accounts for the global contribution of both $tu \rightarrow rs$ (de-excitation) and $rs \rightarrow tu$ (excitation) processes to the population gradient dP_J/dz .

Although MEQ (6) includes a large number of terms, many of them are negligible. In practice, the sum can be truncated to collision processes where the difference of pre- and post-collision rotational energy, $\Delta\epsilon = |\epsilon_t + \epsilon_u - \epsilon_r - \epsilon_s|$, is below a given threshold. Consistently with the experimental thermal range of this work ($T < 300$ K), MEQ (6) has been truncated to $\Delta\epsilon < 1400$ K processes.

Note that in MEQ (6) the dP_J/dz gradients in its left-hand term (LHT) and the number density n , flow velocity v , and b_{turs} coefficients in its right-hand term (RHT) are experimental quantities; S_{Jturs} is the well-defined numerical coefficient given by Equation (7). The k_{turs}^{down} STS rates are the unknowns of the problem. In the present approach they have been taken initially from quantum scattering calculations by Montero et al. (2006) (M06 rates) and by Montero & Pérez-Ríos (2014) (M14 rates). After a preliminary assessment, the latter set has been scaled to the experiment as described below.

Finally, it must be emphasized that MEQ (6) is robust, as it strictly represents the conservation of matter. The MEQ is, however, subject to some approximations, namely, ignoring triple collisions, and radiation emission or absorption. These conditions are well satisfied in the present jet experiments based on nH_2 rarefied media.

3. Results

3.1. Assessing STS Rates

Preexisting STS rates derive in general from closed-coupling (CC) calculations. Such STS rates will be labeled here as k_{turs}^{CC} . In order to test them by means of the experiment, MEQ (6) adopts now the form

$$(dP_J/dz)^{\text{CC}} = \frac{n}{v} \sum_{turs}^* S_{Jturs} b_{turs} k_{turs}^{\text{CC}}, \quad (14)$$

which allows for the comparison of the calculated $(dP_J/dz)^{\text{CC}}$ with the experimental $(dP_J/dz)^{\text{exptl}}$ gradients. How well do the k_{turs}^{CC} STS rates reproduce the $(dP_J/dz)^{\text{exptl}}$ gradients provides clear information about the quality of the assessed STS rates and, indirectly, about the quality of the intermolecular PES employed in the underlying CC calculation.

It must be emphasized that the procedure does not allow assessing the STS rate for a single individual $tu \rightarrow rs$ collision process. Instead, the use of a complete enough set of STS rates is mandatory. Unfortunately, the reported MS80, D87, F98, S06, L08, and W18 rates for $H_2:H_2$ collisions are incomplete sets. As far as we are aware, only the M06 and M14 rates are complete enough sets for $T \leq 300$ K studies of H_2 nonequilibrium media. The set of M06 and M14 rates are assessed here in detail comparing the calculated $(dP_0/dz)^{\text{CC}}$ and $(dP_1/dz)^{\text{CC}}$ gradients with their experimental counterparts.

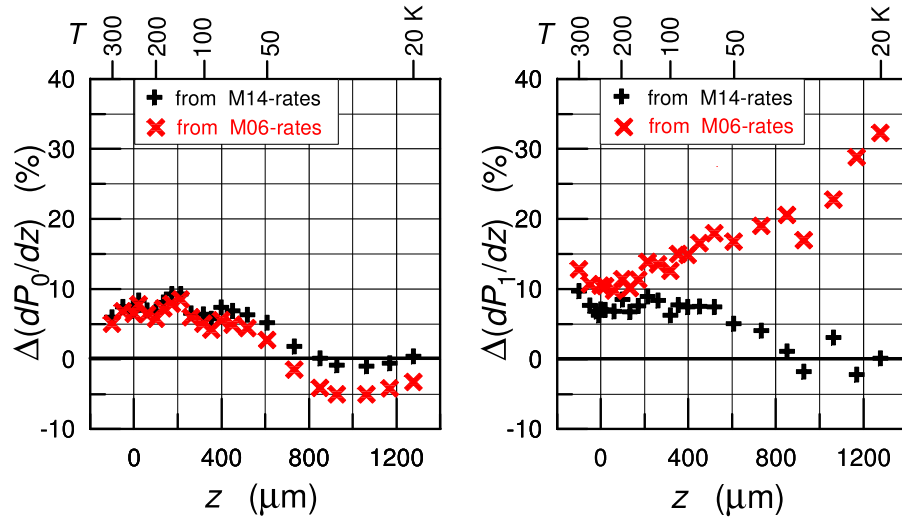


Figure 2. Differences (%) of $(dP_J/dz)^{CC}$ gradients calculated from M06 and M14 rates with respect to the experimental ones.

Figure 2 shows their differences (in %), defined as

$$\Delta(dP_J/dz) = 100((dP_J/dz)^{CC} - (dP_J/dz)^{exptl}) / (dP_J/dz)^{exptl}. \quad (15)$$

The M06 rates assessed in this way against the jet show differences of up to 33% at low temperature for the dP_1/dz gradient. In contrast, both $(dP_0/dz)^{CC}$ and $(dP_1/dz)^{CC}$ gradients calculated from M14 rates show differences below 10% for T between 295 and 60 K and are even closer to the experiment at lower temperatures. The quality of the M14 rates over the M06 rates appears thus quite clear by simple inspection. Consequently, the M14 rates will be employed as the reference for obtaining the improved set of ES rates as described next.

On the other hand, the MS80, D87, F98, S06, L08, and W18 incomplete sets of STS rates cannot be assessed by the procedure described above, but only by comparison with the homologous ES rates as shown in Section 3.3.

3.2. Improving STS Rates

Complete enough sets of STS rates can be improved by means of a scaling procedure described before (Tejeda et al. 2015). This procedure rests on a scaling hypothesis. In this hypothesis it is assumed that in a set of CC-calculated STS rates based on a reasonably good PES

1. the relative values of the same STS rate at two different temperatures, T and T' , i.e., $k_{turs}(T)$ and $k_{turs}(T')$, are more accurate than their individual absolute values; and
2. the relative values of two different rates at the same temperature T , i.e., $k_{turs}(T)$ and $k_{t'ur's'}(T)$, are more accurate than their individual absolute values.

The hypothesis, if true, should lead to a strong correlation between pairs of STS rates from CC calculations based on different PESs, provided that these PESs are of reasonably quality. As a hint in favor of the scaling hypothesis, the pair correlation for D87 and M14 rates, based on different PESs, is shown in Figure 3. The data set includes all common STS rates of D87 and M14 rates reported at temperatures $T = 300, 250, 200, 150, 100$, and 50 K. Abscissa and ordinate display the values of homologous rates according to the values reported by

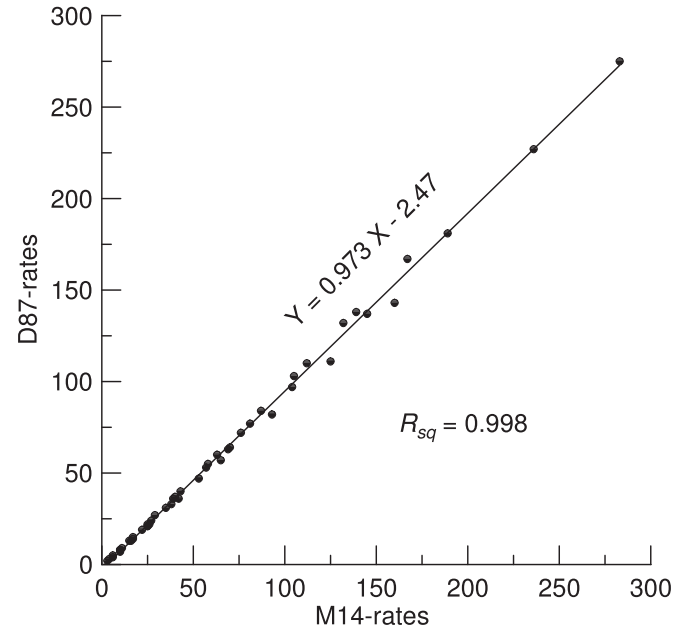


Figure 3. Correlation between D87 rates and M14 rates for $H_2:H_2$ collisions in units of $10^{-20} \text{ m}^3 \text{ s}^{-1}$.

Danby et al. (1987) and Montero & Pérez-Ríos (2014). The $R_{sq} = 0.998$ statistical correlation coefficient of the regression line shown in Figure 3 supports the scaling hypothesis. A similar correlation has been documented in a previous work on $H_2O:He$ collisions (Tejeda et al. 2015). The high correlation strongly suggests that the relative values of each set of STS rates are good enough for scaling to experiment by the procedure described below. It permits us to overcome the problem of the absolute values of the CC-calculated STS rates by scaling. Accordingly, the best one (M14 rates) of the two sets assessed in Section 3.1 will be employed to generate the set of experiment-scaled rates (ES rates) capable of reproducing a great number of observed experimental data with a high degree of accuracy. The ES rates are defined as

$$k_{turs}^{ES}(T) = F(T) \times k_{turs}^{CC}(T), \quad (16)$$

where $F(T)$ is a function common to all STS rates at a given translational temperature T . $F(T)$ only depends on T and is

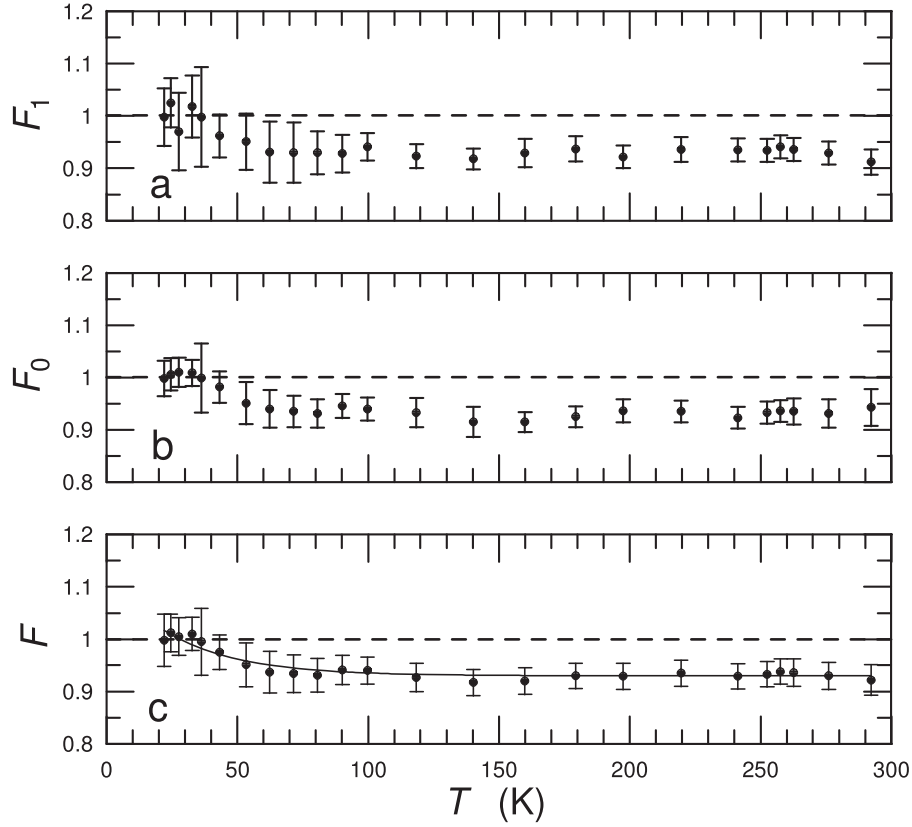


Figure 4. Experimental scaling function $F(T)$ with respect to the CC-calculated M14 rates: (a) $F_1(T)$ from $J = 1$ levels; (b) $F_0(T)$ from $J = 0$ levels; (c) $F(T)$ as the weighted average from $F_0(T)$ and $F_1(T)$.

obtained from calculated and experimental dP_J/dz population gradients. Superscript “down” has been omitted in Equation (16) for simplicity. It must henceforth be understood that only de-excitation STS rates appear in MEQ (6) and later variants. This way, the large number of unknowns in MEQ (6) is reduced to the a priori unknown scaling function $F(T)$. Discrete points of this function are determined in the experiment as follows. Setting the k_{turs}^{ES} s defined in Equation (16) in MEQ (6), we have

$$(dP_J/dz)^{ES} = \frac{n}{v} \sum_{turs}^* S_{Jturs} b_{turs} F_J(T) k_{turs}^{CC}. \quad (17)$$

Since $F_J(T)$ is expected to be common to all $tu \rightarrow rs$ processes, MEQ (17) can be rewritten as

$$(dP_J/dz)^{ES} = \frac{n}{v} F_J(T) \sum_{turs}^* S_{Jturs} b_{turs} k_{turs}^{CC}, \quad (18)$$

or, in short,

$$(dP_J/dz)^{ES} = F_J(T) (dP_J/dz)^{CC}. \quad (19)$$

Since $(dP_J/dz)^{ES}$ are expected to reproduce the $(dP_J/dz)^{exptl}$ gradients as close as possible, i.e., $(dP_J/dz)^{ES} \approx (dP_J/dz)^{exptl}$, the scaling function $F_J(T)$ is obtained as

$$F_J(T) = \frac{(dP_J/dz)^{exptl}}{(dP_J/dz)^{CC}}, \quad (20)$$

where $(dP_J/dz)^{CC}$ is the calculated MEQ (14) for the same position z and temperature $T(z)$ of $(dP_J/dz)^{exptl}$ gradients for all experimentally accessible rotational levels J . Independent

$[T, F_J(T)]$ points are thus obtained from the various rotational levels J at a common position z and temperature $T(z)$.

In a set of (ideal) error-free H_2 jet experiments, using a set of hypothetically exact k_{turs}^{CC} STS rates, i.e., derived from an exact PES, one should obtain $F_J(T) = 1$ for all rotational levels, z -positions, and translational temperatures T in the thermal range of the experiments. In actual experiments combined with CC-calculated STS rates, in general $F_J(T) \neq 1$, with some dispersion for the different rotational levels. In practice, one can take as a best estimate of the scaling function $F(T)$ the average from different J levels and jets. How much departs $F(T)$ from 1, and how large is its dispersion with respect to the mean value, tells us much about the quality of the experimental data and of the reference CC calculation.

Owing to the population relations $P_0 > P_2$, $P_0 \gg P_4$, and $P_1 \gg P_3$ along the jet (see Figure 7(b), Appendix), $(dP_0/dz)^{exptl}$ and $(dP_1/dz)^{exptl}$ are the best-determined gradients. This implies that $F_0(T)$ and $F_1(T)$ leads to the best $F_J(T)$ scaling functions. They are shown in Figure 4 together with its weighted average $F(T)$, which we consider the most accurate scaling function. Weights for $F_0(T)$ and $F_1(T)$ are inversely proportional to the square of their respective uncertainties. Uncertainty bars in Figures 4(a) and (b) have been inferred from the experimental uncertainties of n , v , P_J , and T flow quantities along the jet discussed in the Appendix. The uncertainty bar in Figure 4(c) is the weighted average from the uncertainties in Figures 4(a) and (b). The best-fit function

$$F(T) = 0.93 + 0.19 \exp(-0.0378257 T) \quad (21)$$

(solid line in Figure 4(c)) leads to the ES rates obtained by scaling the M14 rates to the experiment. Its standard deviation

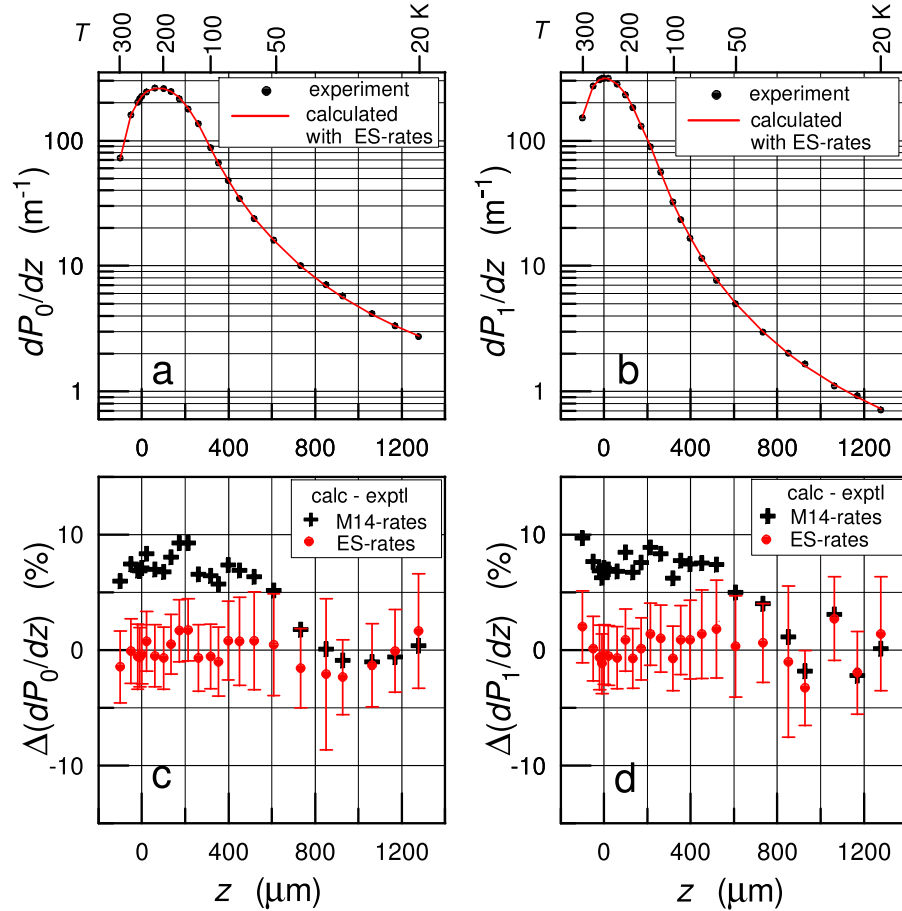


Figure 5. (a, b) $J = 0$ and $J = 1$ population gradients calculated with ES rates (lines) vs. experiment (circles); (c, d) differences (%) with respect to the experiment; 2σ uncertainty bars.

with respect to the $[T, F(T)]$ experimental points is 1% for $20 \text{ K} < T < 295 \text{ K}$. Such a small uncertainty is the result of a large number of spectral data since each data point in Figure 4 is the average of 28 independent measurements for $100 \text{ K} < T < 295 \text{ K}$, and at least 12 measurements under larger acquisition time for $20 \text{ K} < T < 100 \text{ K}$.

The ES rates ($k_{\text{turs}}^{\text{ES}}$) obtained according to Equation (16) are eventually tested against the experiment by means of the MEQ

$$(dP_J/dz)^{\text{ES}} = \frac{n}{v} \sum_{\text{turs}}^* S_{J\text{turs}} b_{\text{turs}} k_{\text{turs}}^{\text{ES}}, \quad (22)$$

which allows comparing calculated versus experimental gradients, i.e., $(dP_J/dz)^{\text{ES}}$ versus $(dP_J/dz)^{\text{exptl}}$ for all J levels. A sample of this result is shown in Figure 5. Figures 5(a) and (b) show the gradients (dP_0/dz) and (dP_1/dz) along the jet, experimental and calculated with ES rates. Figures 5(c) and (d) show the difference (in %)

$$\Delta(dP_J/dz) = 100((dP_J/dz)^{\text{calc}} - (dP_J/dz)^{\text{exptl}}) / (dP_J/dz)^{\text{exptl}} \quad (23)$$

for $J = 0$ and $J = 1$ employing, respectively, M14 rates and ES rates in the calculation with MEQ (22). As shown in Figures 5(c) and (d), the gradients calculated with M14 rates are about 7% larger than the experimental ones for T between 295 and 60 K but agree with the experimental ones within the

experimental uncertainty for T below 60 K. In summary, the $(dP_J/dz)^{\text{ES}}$ gradients calculated with the ES rates agree much better with the experimental ones. The following statistics confirms the high accuracy of the present ES rates along the whole thermal domain 295–20 K:

1. $(dP_0/dz)^{\text{ES}}$ matches the experiment with an average deviation of -0.19% and standard deviation of 1.14% ; extreme deviations are $+1.75\%$ and -2.34% .
2. $(dP_1/dz)^{\text{ES}}$ matches the experiment with an average deviation of $+0.19\%$ and standard deviation of 1.36% ; extreme deviations are $+2.72\%$ and -3.27% .

Slightly lower accuracy is obtained for $(dP_2/dz)^{\text{ES}}$ and $(dP_3/dz)^{\text{ES}}$ gradients, and somewhat lower for $(dP_4/dz)^{\text{ES}}$. Taking into account the large number of experimental data that can be predicted accurately with the ES rates and the accuracy of the experimental data, we estimate a 2σ uncertainty smaller than 3% for the dominant rates k_{2101} , k_{3012} , k_{3111} , and k_{4123} between 295 and 100 K, and up to 6% at 20 K. The accuracy of the remaining STS rates can only be inferred on the basis of the scaling hypothesis owing to their low weight in the calculated $(dP_J/dz)^{\text{ES}}$ gradients shown in the Supplemental Material Tables S2, S3, and S4 (doi:10.20350/digitalCSIC/9015). They bear the highest possible level of information on the inelastic collision problem in an nH_2 jet.

A sample of “down” ES rates and uncertainties obtained as described above is given in Table 1. A more complete set for

Table 1
Experiment-scaled ES Rates for De-excitation H₂:H₂ Inelastic Collisions^a

$tu \rightarrow rs$	ΔE (K)	$T \rightarrow 20$ K $2\sigma \rightarrow 6\%$	40 K 5%	80 K 4%	120 K 3%	160 K 3%	200K 3%	250 K 3%	300 K 3%
20 \rightarrow 00	509.88	38.1	38.9	51.0	67.1	85.2	104.5	129.5	155.3
21 \rightarrow 01	509.88	60.4	62.9	83.7	111.7	142.9	176.1	219.1	263.2
22 \rightarrow 02	509.88	63.8	65.3	85.6	113.1	143.7	176.2	218.3	261.3
23 \rightarrow 03	509.88	65.3	67.2	88.0	116.3	147.9	181.5	225.1	269.5
22 \rightarrow 00	1019.76	0.4	0.5	0.7	1.0	1.5	2.0	3.0	4.0
30 \rightarrow 12	334.82	256.3	270.5	353.6	447.0	536.0	617.6	708.7	789.1
41 \rightarrow 23	327.12	183.7	193.7	252.5	318.6	381.8	439.8	505.2	562.9
41 \rightarrow 03	837.00	0.5	0.5	0.7	0.8	1.1	1.4	1.9	2.2
40 \rightarrow 22	661.94	33.7	37.1	54.8	79.5	108.3	140.2	182.6	226.8
30 \rightarrow 10	844.70	21.7	22.5	31.0	43.4	58.3	75.1	97.9	122.6
31 \rightarrow 11	844.70	20.5	22.2	32.5	47.4	65.7	86.8	116.4	149.2
32 \rightarrow 12	844.70	23.0	24.4	34.5	49.3	67.3	87.9	116.8	148.5
33 \rightarrow 13	844.70	25.3	26.6	37.7	53.7	73.2	95.4	126.4	160.2
40 \rightarrow 20	1171.82	8.0	8.6	12.5	18.6	26.2	35.5	49.0	64.5
41 \rightarrow 21	1171.82	7.8	8.5	12.5	18.9	27.3	37.5	52.7	70.4
42 \rightarrow 22	1171.82	7.8	8.5	12.6	18.9	27.2	37.2	51.6	67.2
32 \rightarrow 10	1354.58	0.4	0.5	0.8	1.1	1.7	2.3	3.3	4.7

Note.

^a 1 K = 0.69504 cm⁻¹; ES rates in units of 10⁻²⁰ m³ s⁻¹; estimated 2 σ uncertainty in %.

(This table is available in its entirety in machine-readable form.)

the 300–20 K range, including also “up” ES rates, is given in the online MRF-Table 1. Though the actual experiment runs from 295 to 20 K, the smooth behavior of the $F(T)$ scaling function and of the M14 rates allows for a safe extrapolation to 300 K, more convenient for tabulation purposes. A parametric description of the “down” ES rates based on the power series

$$k_{turs}(T) = \sum_{m=0}^{m=4} a_m T^m \quad (24)$$

allows for interpolation between 20 and 300 K with accuracy better than 0.5%. Though less accurate, the Arrhenius-Kooij equation (Vissapragada et al. 2016),

$$k_{turs}(T) = A \left(\frac{300}{T} \right)^{-B} \exp \left(\frac{-C}{T} \right), \quad (25)$$

also provides a description of the “down” ES rates between 20 and 300 K and allows for a plausible extrapolation up to 1000 K as inferred from comparison with theoretical results (Lee et al. 2008; Wan et al. 2018). Parameters a_m for Equation (24) and A, B, and C for Equation (25) are given in the MRF-Table included in doi:10.20350/digitalCSIC/9015 and in the .tar.gz package.

All calculations described above involving the MEQ have been run with the MEQHH19.FOR Fortran 77 code (Montero 2019) plus nH2-19.MEQ input file. This file includes a great number of experimental data.

3.3. Comparing with Previous STS Rates

A summary of STS rates for H₂:H₂ inelastic collisions calculated previously by different authors has been reported by Montero & Pérez-Ríos (2014, Table XI). Comparison with the present ES rates of MRF-Table 1 is pertinent. Figure 6 shows the percentage differences $\Delta k_{turs} = 100(k_{turs}^{CC} - k_{turs}^{ES})/k_{turs}^{ES}$ for

the k_{turs} de-excitation rates available in the literature with respect to the present ES rates.

The first experimental determination of an STS rate for pH₂:pH₂ collisions at low temperature by Maté et al. (2005) has also been included in Figure 6(c) (Δk_{2000}) for comparison. Here the k_{2000} de-excitation rate is derived from the original k_{0020} excitation rate, which has often been employed in the literature as a reference for CC calculations. Such comparisons of calculated versus experimental k_{0020} excitation rate are somewhat misleading since k_{0020} strongly depends on temperature. From 300 to 20 K the k_{0020} excitation rate decreases by 11 orders of magnitude. Graphic comparison in such a wide range requires a logarithmic scale that easily camouflages a difference of 50% or smaller. This led to the perception that the agreement between calculated and experimental k_{0020} rate was better than it actually was. For this reason the comparison should be done in terms of de-excitation STS rates, which are far less dependent on temperature. This allows for a linear scale where the k_{2000} de-excitation rate spans less than one order of magnitude for T between 300 and 20 K as shown in Table 1 and MRF-Table 1. Therefore, Figure 6 is plotted in terms of de-excitation rates that have been transformed from the published excitation rates by means of the detailed balance Equation (3).

Figure 6(c) shows that the experimental k_{2000} by Maté et al. (2005) is up to 45% too large compared to the present k_{2000} ES rate, which is expected to be far more accurate. CC-calculated D87, M06, L08, and M14 rates compared with the present k_{2000} ES rate are well within 10% between 300 and 20 K as shown in Figure 6(c). The F98 and S06 rates show differences of up to 18%, and the MS80 rate has still larger differences with respect to the present k_{2000} ES rate.

In addition to the k_{2000} rate, reported CC calculations of the k_{2101} , k_{3012} , and k_{3111} rates are compared to the homologous ES rates in Figures 6(a), (b), and (d). Although k_{2101} is about 60%

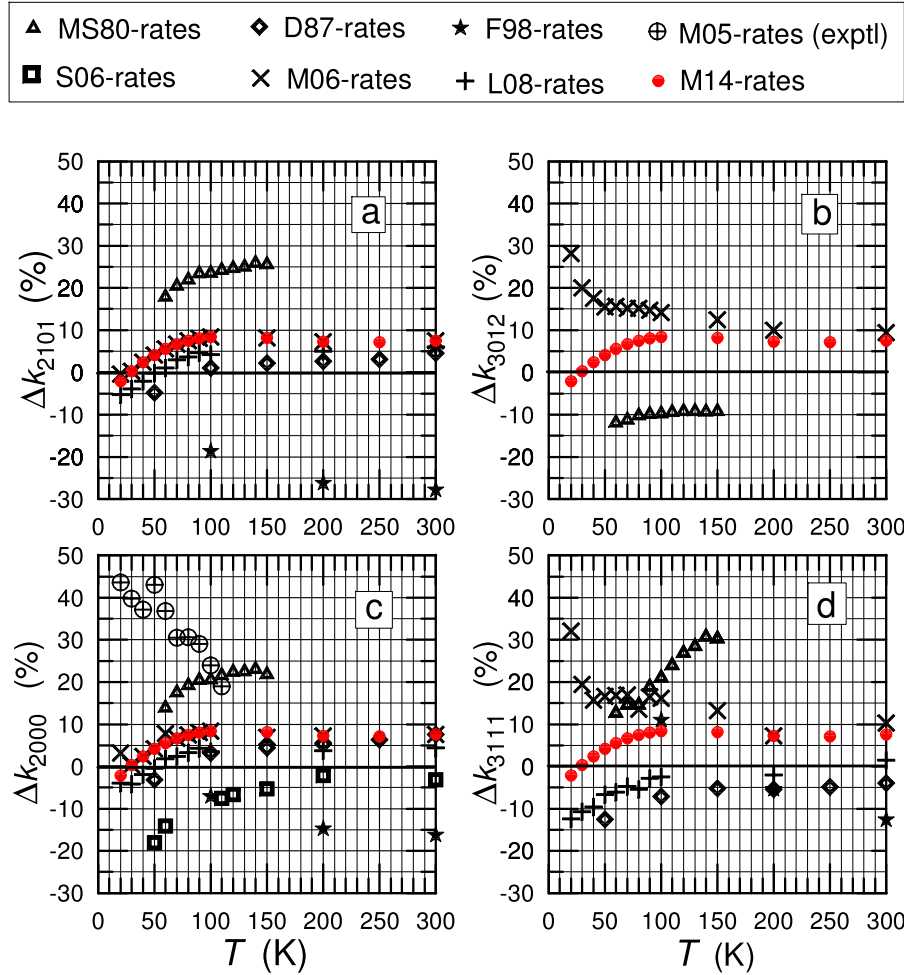


Figure 6. Differences (%) of CC-calculated rates with respect to the ES rates.

larger than k_{2000} , the differences with respect to the k_{2101} ES rate show a similar behavior; calculated **D87**, **M06**, **L08**, and **M14** rates are within 10% of k_{2101} ES rate as shown in Figure 6(a), while **MS80** and **F98** rates are outside of this threshold.

Comparison of k_{3012} and k_{3111} rates with the homologous ES rates bears some surprises. The **M06**-, **L08**-, and **M14**- k_{3111} rates shown in Figure 6(d) are clearly different, notwithstanding that the same **DJ00**-PES and **MOLSCAT** methodology was employed in all three calculations. However, the **D87**- and **L08**- k_{3111} rates, which are based on different PESs, agree within 5%, as happens with the k_{2000} and k_{2101} rates. This suggests the high quality of **D87** and **L08** calculations and underlying **MSL80**- and **DJ00**-PES, respectively.

As shown in Figure 6(b), the **M06**- and **M14**- k_{3012} rates diverge at low temperatures. This discrepancy, which concerns the $J = 3$ excited rotational level, deserves further numerical investigation. The **MS80**- k_{3012} rate is 10% smaller than the corresponding ES rate, in contrast with the k_{2000} , k_{2101} , and k_{3111} , which are up to 20% larger.

An intriguing question is the systematic decreasing trend of the Δk_{turs} differences shown in Figure 6 for $T < 100$ K. In principle, this trend cannot be attributed to limitations of the PESs employed since CC calculations based on different PESs show a similar behavior. Neither does it seem possible to attribute this effect to systematic errors in the experimental data

in view of the accuracy of the results in Figures 4 and 5. In any case, this question remains open and requires further investigation.

STS rates for $\text{H}_2\text{:H}_2$ inelastic collisions described by means of polynomial functions in the pioneer work of Green et al. (1978) suffer from the truncation of cross sections to collision energies below 500 K. As shown in Table 2, the dominant rates hardly match the right order of magnitude compared to the present dominant ES rates between 20 and 300 K.

W18 rates have been reported graphically and do not allow for an accurate comparison with the present ES rates. A semiquantitative comparison based on Figure 6 of Wan et al. (2018) suggests that the reported k_{2000} , k_{2101} , k_{3010} , and k_{3111} rates are slightly lower than the present ES rates.

Finally, CC calculations based on full-dimensional PESs deserve some mention. The **O08**- k_{0020} rate based on **B02**-PES was about five times smaller than the first experimental value of k_{0020} by Maté et al. (2005) and about 4.5 times smaller than the present ES rate. The k_{0020} of **B11a** rates, which were also based on **B02**-PES, did show a similar behavior, while **B11b** rates based on **H08**-PES were about twice as large. Both results, once converted to “down” rates, are beyond the scale of Figure 6(c). The **L02** rates, also based on **B02**-PES, were reported at temperatures too high for comparison with the present experiment.

Table 2
Green et al. (1978) Excitation Rates Compared to the Experiment-scaled ES Rates^a

$tu \rightarrow rs$	$T \rightarrow$	20 K	50 K	100 K	200 K	300 K
00 \rightarrow 20	Green78	0.2735E-27	0.8546E-21	0.1195E-18	0.1533E-17	0.3992E-17
	ES rate	0.1615E-28	0.7680E-22	0.1794E-19	0.4080E-18	0.1419E-17
	ratio	16.93	11.12	6.66	3.76	2.81
01 \rightarrow 21	Green78	0.1747E-27	0.5385E-21	0.7363E-19	0.9104E-18	0.2306E-17
	ES rate	0.2561E-28	0.1247E-21	0.2963E-19	0.6878E-18	0.2405E-17
	ratio	6.82	4.32	2.49	1.33	0.96
02 \rightarrow 22	Green78	0.2633E-27	0.7990E-21	0.1065E-18	0.1257E-17	0.3062E-17
	ES rate	0.2703E-28	0.1289E-21	0.3011E-19	0.6882E-18	0.2388E-17
	ratio	9.74	6.20	3.54	1.83	1.28
12 \rightarrow 30	Green78	0.7618E-25	0.1240E-20	0.2990E-19	0.1572E-18	0.3009E-18
	ES rate	0.6416E-25	0.1661E-20	0.6568E-19	0.5403E-18	0.1206E-17
	ratio	1.19	0.75	0.46	0.29	0.25
11 \rightarrow 31	Green78	0.1392E-34	0.9441E-24	0.3436E-20	0.2014E-18	0.8088E-18
	ES rate	0.2173E-36	0.2595E-25	0.1974E-21	0.2966E-19	0.2084E-18
	ratio	64.06	36.38	17.41	6.79	3.88
13 \rightarrow 33	Green78	0.2200E-34	0.1477E-23	0.5276E-20	0.2983E-18	0.1158E-17
	ES rate	0.2681E-36	0.3089E-25	0.2264E-21	0.3261E-19	0.2238E-18
	ratio	82.06	47.81	23.30	9.15	5.17

Note.

^a Excitation rates in units of $\text{m}^3 \text{s}^{-1}$.

4. Remarks and Conclusions

In this work the $\text{H}_2\text{:H}_2$ inelastic collisions have been studied experimentally in supersonic jets probed by Raman spectroscopy. The probed gas volume \mathcal{R} (Figure 1) shares features in common with regions of the interstellar medium. First, by virtue of the gasdynamic properties along the paraxial region of the supersonic jet, the molecules are self-confined and free from interaction with cell walls or with other warmer or colder molecules traveling upstream or downstream of the probed gas volume \mathcal{R} . Second, the supersonic expansion provides an efficient way of cooling the target molecules, in this case pH_2 and oH_2 molecules, from the nozzle stagnation conditions down to temperatures that are out of the possibilities of static-gas techniques. As an additional advantage of the methodology, all flow-related quantities (local rotational populations and their derivatives, number density, temperatures, and flow velocity) are smoothly correlated with the distance z of the probed volume \mathcal{R} to the nozzle. This enables using efficient numerical methods to improve the accuracy of the measured quantities by means of suited functional descriptions as explained in the Appendix. Finally, since the Raman scattering cross sections are very small, the perturbation of the probed gas volume \mathcal{R} by the laser beam is negligible.

As a main result of the present study, a set of STS rates for $\text{pH}_2\text{:pH}_2$, $\text{pH}_2\text{:oH}_2$, and $\text{oH}_2\text{:oH}_2$ inelastic collisions between 300 and 20 K has been established on an experimental basis. The high accuracy of the spectroscopic data on which the work is based, jointly with the improved methodology, has rendered up STS rates with 2σ uncertainty between $\approx 3\%$ at 300 K and $\approx 6\%$ at 20 K.

The present results also prove that the thermal nonequilibrium problem in H_2 media does not allow for simplifications. The kinetic master equation (MEQ) that governs the evolution of rotational populations by means of inelastic collisions is indeed intricate and depends strongly on the local conditions of the medium, i.e., on their macroscopic thermodynamic variables. This can be inferred from Tables S2, S3,

and S4 included in the Supplemental Material (doi:10.20350/digitalCSIC/9015). Among other features, they reveal the strong nonlinearity of the collisional problem, which essentially depends on the local breakdown of rotational-translational thermal equilibrium. As shown in Figure 7(c), this is extremely small (<0.1 K) at the onset of the expansion near 300 K, but very large (≈ 110 K) at farther downstream points of the jet at $T \approx 20$ K. At the onset this dependence is highly nonlinear, but later, as the translational temperature decreases below 100 K, the MEQ tends to turn into a linear behavior. The fact that all the experimental quantities (z , n , P_J , dP_J/dz , T , v) along the jet are combined in the MEQ with the STS rates along a wide range of conditions spanning orders of magnitude leads to highly consistent and robust results.

Some interesting topics on the thermal nonequilibrium problem in H_2 media that were not considered at the beginning of this work but have emerged later have been included in the Supplemental Material in doi:10.20350/digitalCSIC/9015 owing to their potential interest.

Although the main text and Supplemental Material of the present work might look too detailed in some steps, we prefer to report it in this way since H_2 jets provide the unique molecular medium where the inelastic collision problem can be studied at the highest level of detail both experimentally and in the frame of first-principle quantum scattering calculations. Astrophysical use of the STS rates in the matter-radiation balance equation should take into account some of the features reported here.

Finally, this work will be useful for the in-progress study of $\text{H}_2\text{O:H}_2$ collisions in our laboratory. Since this is based on highly diluted jets of H_2 seeded with small ($\approx 0.2\%$) amounts of H_2O , a detailed knowledge of the hydrodynamic and collisional behavior in pure H_2 jets is mandatory.

We are indebted to the referees for the useful comments that helped us improve the paper. This work has been supported by the Spanish Ministerio de Ciencia e Innovación (MICINN) and Economía y Competitividad (MINECO) through the

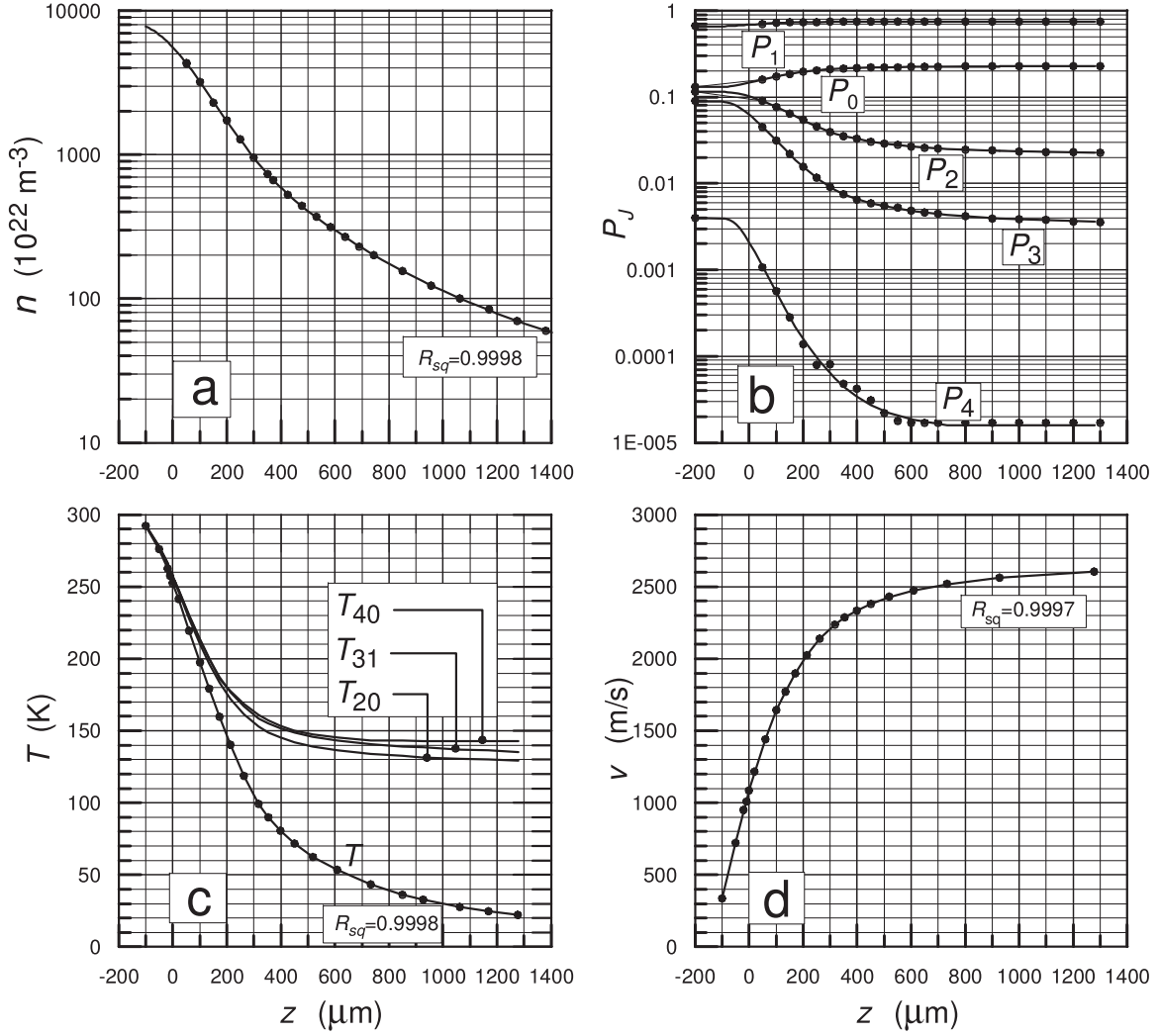


Figure 7. Sample of raw (circles) and processed data (lines) of the $\text{nH}_2\text{-3288}$ jet. Flow quantities: z is the distance along the jet, n the number density, P_J the populations of rotational levels, T the translational temperature, T_{40} , T_{31} , and T_{20} the pairwise rotational temperatures, and v the flow velocity.

research projects CONSOLIDER ASTROMOL CSD2009-0038, FIS2010-22064-C01, FIS2013-48275-C2-2-P, and FIS2017-84391-C2-1-P.

Appendix

A.1. Experimental

The experimental investigation of STS rates for $\text{H}_2\text{:H}_2$ inelastic collisions at translational temperatures $T(z)$ between 295 and 20 K in a single experiment based on steady nH_2 supersonic jets poses a number of challenges. The first has to do with the supersonic flow conditions compatible with the instrumental limitations such as geometrical size and space resolution along and across the flow field, spectral sensitivity, pumping speed of the vacuum system, safety, and others. Supersonic expansions in the 295–20 K range convey a decrease of the local number density $n(z)$ along the flow field of more than two orders of magnitude. This constraint, imposed by the gasdynamic conservation laws of mass, momentum, and energy, is unavoidable. Simultaneous rotational cooling imposes a dynamical range of over four orders of magnitude to the rotational populations $P_J(z)$. In the whole, the number of H_2 molecules to be quantified spectroscopically spans over six

orders of magnitude, depending on the point z of the flow field and on the rotational level J as can be inferred from Figures 7(a) and (b). These constraints pose a limit to the accuracy and even to the feasibility of spectral quantitative measurements.

Raman scattering as employed here is so far the only technique capable of providing the accurate number densities $n(z)$, rotational populations $P_J(z)$, and dP_J/dz gradients for the MEQ. It has the advantage of its superb space resolution, time stability, and linearity of more than six orders of magnitude, but the disadvantage of its relatively low sensitivity. It requires a number of molecular scatterers as high as possible. This number can be increased by augmenting the stagnation pressure p_0 of the expansion and the diameter D of the nozzle. But this enters in conflict with the required vacuum conditions of the expansion chamber, i.e., with the pumping speed of the vacuum system. By trial and error we have found the operational limit of our apparatus in $p_0 \times D^2 < 0.4 \text{ bars mm}^2$ for nH_2 jets. With this figure in mind we have chosen $D \approx 350 \mu\text{m}$ nozzles for the several runs of the present experiment. This allows for high space resolution measurements as close to the nozzle exit as $D/7 \approx 50 \mu\text{m}$. Such a close distance to the nozzle exit, never reached before in laboratory jets as far as we are aware, is the key to spanning the

thermal domain above 100 K. The stagnation pressure of the jets is limited to $p_0 \approx 3.3$ bars by virtue of the $p_0 \times D^2$ limit.

The data set for the present work has been generated along a number of 1-day sessions, often separated in time by months. Since the stagnation pressure and temperature may vary slightly from session to session, and different nozzles have been employed, the jets of different runs have been reduced to a common reference jet at $p_0 = 3288$ mbar, $T = 295.4$ K, and $n_0 = 8063 \times 10^{22} \text{ m}^{-3}$ nominal stagnation conditions, and to a common $D = 345.6 \mu\text{m}$ reference nozzle. This reduction, which is aimed at a better consistency of data from different runs, is based on the dynamic similarity properties of supersonic jets. Therefore, along the paper all jets are referred to as “the jet.”

A.2. Measured Quantities

The flow field of the jet is indeed very small. The scheme of Figure 1 is drawn to scale, approximately. Laser beam and volume \mathcal{R} of Figure 1 are kept fixed in space, while nozzle and flow field are displaced by high-precision xyz -platforms ($0.1 \mu\text{m}$ repeatability) to align xy -positions and to fix distance z . The quantities measured in the volume \mathcal{R} can be classified in two groups. The first group includes the primary quantities, which are those obtained directly from the experiment. These are the distance z from nozzle exit to observed volume \mathcal{R} , the local number densities $n(z)$, and the rotational populations $P_J(z)$. As explained below, $n(z)$ and $P_J(z)$ are measured from the intensity of the Raman spectral lines collected along the Y -direction. Distance z appears implicitly everywhere in the MEQ, while $n(z)$ and $P_J(z)$ appear explicitly in its RHT. The second group includes the quantities derived from the primary ones by indirect methods. These quantities are the dP_J/dz population gradients, the translational temperature $T(z)$, and the flow velocity $v(z)$; $dP_J(z)/dz$ and $v(z)$ appear, respectively, in the LHTs and RHTs of MEQ (5) and successive variants: $T(z)$ is implicit in the STS rates of the RHT.

Local number densities $n(z)$ were measured along the jet from the integrated intensity of the $Q(\nu_1)$ Raman band spanning from 4100 up to 4165 cm^{-1} (Figure 8) by comparison with a reference static sample of nH_2 at $p_{\text{ref}} = 50.2 \pm 0.1$ mbar in the expansion chamber. Populations $P_J(z)$ were obtained from the relative intensities $I_J(z)$ of the individual $(v = 0, J) \rightarrow (v = 1, J)$ Raman lines measured at positions z .

Rotational populations and intensities are related by

$$I_J(z) = C(J) \left[\langle 0J|\bar{\alpha}|1J \rangle^2 + \frac{7}{45} \frac{J(J+1)}{(2J-1)(2J+3)} \langle 0J|\gamma|1J \rangle^2 \right] P_J(z), \quad (26)$$

where $\bar{\alpha}$ and γ are, respectively, the mean polarizability and the anisotropy invariants of molecular hydrogen. The values of the invariant moments (in units of $10^{-42} \text{ CV}^{-1} \text{ m}^2$) employed here,

$$\begin{aligned} \langle 00|\bar{\alpha}|10 \rangle &= 12.902, & \langle 00|\gamma|10 \rangle &= 0, \\ \langle 01|\bar{\alpha}|11 \rangle &= 12.952, & \langle 01|\gamma|11 \rangle &= 11.056, \\ \langle 02|\bar{\alpha}|12 \rangle &= 13.053, & \langle 02|\gamma|12 \rangle &= 11.129, \\ \langle 03|\bar{\alpha}|13 \rangle &= 13.203, & \langle 03|\gamma|13 \rangle &= 11.238, \\ \langle 04|\bar{\alpha}|14 \rangle &= 13.403, & \langle 04|\gamma|14 \rangle &= 11.384, \end{aligned} \quad (27)$$

were obtained in our laboratory from static Raman measurements on nH_2 . For $J = 0, 1, 2$ the estimated uncertainty of

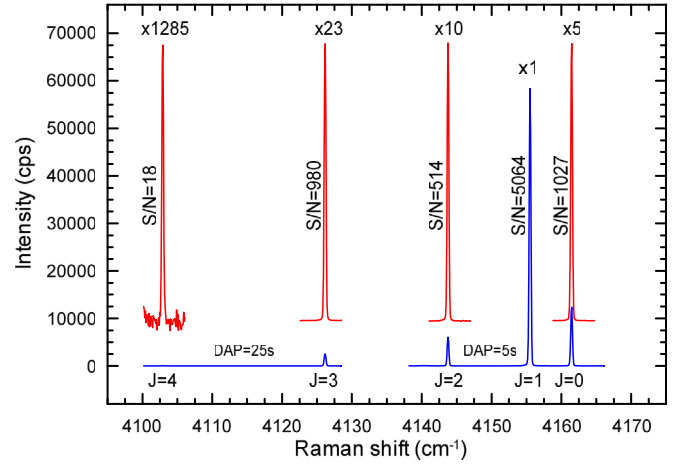


Figure 8. Representative sample spectrum of the nH_2 -3288 jet recorded at $z = 100 \mu\text{m}$.

$\langle 0J|\bar{\alpha}|1J \rangle$ is 0.5%; for $J = 3$ it is 1.0%, and for $J = 4$ it is 2%. Uncertainty is twice as much for $\langle 0J|\gamma|1J \rangle$, but their weight is far smaller. The moments agree well with recent high-level ab initio calculations (Raj et al. 2018); $C(J)$ is a very nearly constant factor fixed a posteriori by the normalization of the populations. From Equations (26) and (27) the populations $P_J(z)$ are obtained from Raman intensities $I_J(z)$ as

$$\begin{aligned} P_0(z) &= K(z) 1.05314 I_0(z), & P_1(z) &= K(z) 1.00000 I_1(z), \\ P_2(z) &= K(z) 0.99260 I_2(z), & P_3(z) &= K(z) 0.96782 I_3(z), \\ P_4(z) &= K(z) 0.93469 I_4(z), \end{aligned} \quad (28)$$

where $K(z)$ is fixed at each z position by the normalization conditions $P_0(z) + P_2(z) + P_4(z) = 0.25$ and $P_1(z) + P_3(z) = 0.75$, which hold along the expansion. Intensities $I_J(z)$ in Equation (28) have been corrected previously by the local sensitivity of the CCD detector under the particular binning conditions of the experiment. Along the present work we have found differences in sensitivity of up to 12% between the binned pixels corresponding to the $J = 0, \dots, 4$ spectral lines. Correction of these inhomogeneities is mandatory for the accuracy of the populations $P_J(z)$ required in this work. The $n(z)$ and $P_J(z)$ primary data were measured at discrete steps $\Delta z = 50 \mu\text{m}$ for $50 \mu\text{m} \leq z \leq 350 \mu\text{m}$ with a binning of 7×3 pixels, and $\Delta z = 100 \mu\text{m}$ for $350 \mu\text{m} < z \leq 1600 \mu\text{m}$ with a binning of 133×3 pixels. Sectioning of the volume \mathcal{R} image onto the CCD in 7-pixel strips, equivalent to a resolution of ca $9 \mu\text{m}$ each across the jet, is an important experimental novelty introduced here. Such high space resolution permits us to locate the flow axis with unprecedented accuracy in the paraxial region of the jet. This is of primordial importance in the near flow field region, $z < 2D/3$, where the cross section of the flow displays a sharp bell-like profile, the sharper the closer to the nozzle exit.

Several runs, each one with up to 20 spectra, were accumulated at each position z ; typical accumulation time was 90 s. A summary of $n(z)$ and $P_J(z)$ data is shown in Figures 7(a) and (b).

The local translational temperature $T(z)$ and flow velocity $v(z)$ along the jet were determined by integration of the Navier–Stokes equations for the paraxial zone of the jets, constrained by the

primary experimental data, $n(z)$ and $P_f(z)$, according to the procedure described elsewhere (Montero 2017, Equations (35)–(37)). For the paraxial region of the jet this solution provides a very good approximation. It is, however, subject to some uncertainty due to the dissipation function \mathcal{D} (Montero 2013, 2017) associated with the large bulk viscosity of $n\text{H}_2$. This effect is important in jets generated at low pressure. However, in the case of the present reference jet at $p_0 = 3288$ mbar it just increases the translational temperature by about 2 K with respect to a purely isentropic expansion. The effect of \mathcal{D} on the flow velocity is negligible in this case. Translational temperature and flow velocity along the jet are shown in Figures 7(c) and (d). Since the paraxial zone of the jet is laminar, the local flow velocity and the distance z provide a high-accuracy timescale in the domain of nanoseconds, which allows for the link between MEQs (1) and (5). The pairwise rotational temperatures T_{20} , T_{40} , and T_{31} of Equations (10) and (11) are included in Figure 7(c) for comparison.

A.3. Data Management

As important as the accuracy of the raw experimental data is the proper handling of them for noise reduction and accurate determination of the dP_f/dz gradients, which are compared to the calculated ones in the frame of the MEQ. The use of sigmoid functions of the type

$$Y(z) = c + (Y_0 - c) \times \exp(-b/(z + z_0)^a),$$

$$a < 0, \quad b > 0, \quad c \neq 0 \quad (29)$$

for the near-field flow ($z < 2D/3$) and

$$Y(z) = Y_0 + c \times \exp(-b/(z + z_0)^a),$$

$$a > 0, \quad b > 0, \quad c \neq 0 \quad (30)$$

for the middle- and far-field flow ($z > 2D/3$) is suitable for this purpose; z_0 is the origin of the expansion. Such functions and their derivatives provide highly accurate local approximations to the exact solution of Navier–Stokes equations. The only exception to this behavior is the number density at $z \geq 2D/3$, which obeys a generic function of the type

$$n(z) = b/(c + (z - a)^2), \quad (31)$$

describing the trend toward radial flow lines. For $n(z)$, functions (29) and (31) do overlap smoothly at $z \approx 2D/3$. They provide excellent accuracy, usually with mean square regression values $R_{\text{sq}} > 0.999$ with respect to the raw experimental data as shown in Figure 7(a).

The (dP_f/dz) population gradients along the jet cannot be obtained with sufficient accuracy from the raw $P_f(z)$ data. Derivatives of functions (29) and (30) allow for the best determinations of (dP_f/dz) .

Among other merits, functions (29) and their derivatives allow for interpolation between the first experimental data point at $z = 50 \mu\text{m}$ and the stagnation conditions at the origin z_0 of the expansion. This allows for data in the thermal range $200 \text{ K} < T < 295 \text{ K}$ in the flow domain $z_0 \mu\text{m} < z < 50 \mu\text{m}$, which is not accessible to direct measurements.

Samples of experimental and processed data from the $n\text{H}_2$ -3288 reference jet are shown in Figure 7. Circles in Figures 7(a) and (b) stand for the raw primary data of $n(z)$ and $P_f(z)$; circles in Figures 7(c) and (d) are Navier–Stokes solutions for $T(z)$ and $v(z)$; solid lines are the analytical description according to Equations (29)–(31). The estimated 2σ uncertainty of the processed data is as follows: $\Delta n(z) = 1\%$

along the whole domain z ; $\Delta P_0(z) = 0.2\%$, $\Delta P_1(z) = 0.1\%$, $\Delta P_2(z) = 1\%$, $\Delta P_3(z) = 2\%$, $\Delta P_4(z) = 4\%$; $\Delta T(z) = 0.6\%$ in the near-field region and up to 5% in the far-field region; $\Delta v(z) = 1\%$ along the whole flow field.


A.4. Instrumentation

The experimental work has been conducted in a dedicated facility for quantitative gas-diagnostics at the Laboratory of Molecular Fluid Dynamics (IEM-CSIC, Madrid). A description of the main apparatus can be found elsewhere (Tejeda et al. 2015). It is based on an expansion chamber of ~ 80 liters in volume, which is evacuated by a 2000 l s^{-1} turbopump backed by Roots and rotary pumps. In the expansion chamber the supersonic jet of each run was produced by expanding 99.999% purity $n\text{H}_2$ through the nozzle. As shown in Figure 1, the Raman scattering from volume \mathcal{R} was excited by the sharply focused beam ($15 \mu\text{m}$) of a single-mode Coherent-VERDI V10 cw laser delivering 10 W at $\lambda = 532 \text{ nm}$. The scattering collected along the Y -axis was analyzed by a 1 m grating double-monochromator of $\approx 0.1 \text{ cm}^{-1}$ spectral resolution. The spectrometer is equipped with a CCD camera refrigerated at -120°C by liquid N_2 . This allows for a very low noise level and guarantees a high signal-to-noise ratio (S/N) along the experiment. Representative S/N values of a single spectrum are shown in the sample spectrum of Figure 8. Spectral accumulation and data processing lead to the flow data for the MEQ shown in Figure 7 (lines). They are about one order of magnitude more accurate than in any previous work. Present instrumentation and working conditions represent the state of the art of quantitative measurements in supersonic jets.

ORCID iDs

S. Montero  <https://orcid.org/0000-0003-2795-4384>

G. Tejeda  <https://orcid.org/0000-0003-0810-9652>

J. M. Fernández  <https://orcid.org/0000-0002-6636-7978>

References

- Aguado, A., Suarez, C., & Paniagua, M. 1994, *JChPh*, **101**, 4004
- Anikin, Yu. A. 2017, *CMMPh*, **57**, 1048
- Arthurs, A. M., & Dalgarno, A. 1960, *RSPSA*, **256**, 540
- Audibert, M.-M., Joffrin, C., & Ducuing, J. 1974, *CPL*, **25**, 158
- Audibert, M.-M., Vilaseca, R., Lukasik, J., & Ducuing, J. 1975, *CPL*, **31**, 232
- Balakrishnan, N., Quemener, G., Forrey, R. C., Hinde, R. J., & Stancil, P. C. 2011, *JChPh*, **134**, 014301
- Bohr, A., Paolini, S., Forrey, R. C., Balakrishnan, N., & Stancil, P. C. 2014, *JChPh*, **140**, 064308
- Boothroyd, A. I., Martin, P. G., Keogh, W. J., & Peterson, M. J. 2002, *JChPh*, **116**, 666
- Dalgarno, A. 2000, in *Molecular Hydrogen in Space*, ed. F. Combes & G. Pineau des Forets (Cambridge: Cambridge Univ. Press), 3
- Danby, G., Flower, D. R., & Monteiro, D. R. 1987, *MNRAS*, **226**, 739
- Davison, W. D. 1962, *Disc. Farad. Soc.*, **33**, 71
- Diep, P., & Johnson, J. K. 2000, *JChPh*, **112**, 4465
- Flower, D. R. 1998, *MNRAS*, **297**, 334
- Flower, D. R. 2000, *JPhB*, **33**, 5243
- Flower, D. R., Bourhis, G., & Launay, J. M. 2000, *CoPhC*, **131**, 187
- Fonseca dos Santos, S., Balakrishnan, N., Forrey, R. C., & Stancil, P. 2013, *JChPh*, **138**, 104302
- Fonseca dos Santos, S., Balakrishnan, N., Lepp, S., et al. 2011, *JChPh*, **134**, 214303
- Gatti, F., Otto, F., Sukiasyan, S., & Meyer, H. D. 2005, *JChPh*, **123**, 174311
- Green, S. 1975, *JChPh*, **62**, 2271
- Green, S., Ramaswamy, R., & Rabitz, H. 1978, *ApJS*, **36**, 483
- Habart, E., Walmsley, C. M., Verstraete, L., et al. 2005, *SSRv*, **119**, 71
- Hermans, P. W., Hermans, L. J. F., & Beenakker, J. J. M. 1983, *PhyA*, **122**, 173

- Hinde, R. J. 2008, [JChPh](#), **128**, 154308
- Hutson, J. M., & Green, S. 1994, Molscat Computer Code v14 (Swindon: UK Sci. Engin. Res. Council)
- Köhler, W. E., & Schaefer, J. 1983, [JChPh](#), **78**, 6602
- Krems, R. V. 2006, TwoBC, Quantum Scattering Program (Vancouver: Univ. British Columbia)
- Kühnel, M., Fernández, J. M., Tejeda, G., et al. 2011, [PhRvL](#), **106**, 245301
- Lee, T.-G., Balakrishnan, N., Forrey, R. C., et al. 2006, [JChPh](#), **125**, 114302
- Lee, T.-G., Balakrishnan, N., Forrey, R. C., et al. 2008, [ApJ](#), **689**, 1105
- Le Flohic, M. P., Duggan, P., Sinclair, P. M., Drummond, J. R., & May, A. D. 1994, [CaJPh](#), **72**, 186
- Lin, S. Y., & Guo, H. 2002, [JChPh](#), **117**, 5183
- Maté, B., Thibault, F., Tejeda, G., Fernández, J. M., & Montero, S. 2005, [JChPh](#), **122**, 064313
- Monchick, L., & Schaefer, J. 1980, [JChPh](#), **73**, 6153
- Montero, S. 2013, [PhFl](#), **25**, 056102
- Montero, S. 2017, [PhFl](#), **29**, 096101
- Montero, S. 2019, MEQHH19.FOR Fortran 77 Code Plus nH2-19.MEQ
- Montero, S., & Pérez-Ríos, J. 2014, [JChPh](#), **141**, 114301
- Montero, S., Thibault, F., Tejeda, G., & Fernández, J. M. 2006, [JChPh](#), **125**, 124301
- Otto, F., Gatti, F., & Meyer, H. D. 2008, [JChPh](#), **128**, 064305
- Panda, A. N., Otto, F., Gatti, F., & Meyer, H. D. 2007, [JChPh](#), **127**, 114310
- Patkowski, K., Cencek, W., Jankowski, P., et al. 2008, [JChPh](#), **129**, 094304
- Pérez-Ríos, J., Tejeda, G., Fernández, J. M., Hernández, M. I., & Montero, S. 2011, [JChPh](#), **134**, 174307
- Quemener, G., & Balakrishnan, N. 2009, [JChPh](#), **130**, 114303
- Rabitz, H., & Lam, S. 1975, [JChPh](#), **63**, 3532
- Rahn, L. A., Farrow, R. L., & Rosasco, G. L. 1991, [PhRvA](#), **43**, 6075
- Raj, A., Hamaguchi, o-H., & Witek, H. A. 2018, [JChPh](#), **148**, 104308
- Roberts, C. S. 1963, [PhRv](#), **131**, 209
- Schaefer, J. 1994, [A&A](#), **284**, 1015
- Schaefer, J. 2010, [ChPhy](#), **368**, 38
- Schaefer, J., & Köhler, W. E. 1989, [ZPhyD](#), **13**, 217
- Schwenke, D. W. 1988, [JChPh](#), **89**, 2076
- Semenov, A., & Babikov, D. 2016, [JPCA](#), **120**, 3861
- Snider, R. F. 1998, [IRPC](#), **17**, 185
- Sternberg, A., & Dalgarno, A. 1989, [ApJ](#), **338**, 197
- Sultanov, R. A., & Guster, D. 2006, [ChPhy](#), **326**, 641
- Takayanagi, K. 1959, Sc. Repts. Saitama Univ. A, **3**, 87
- Takayanagi, K. 1965, [AdAMP](#), **1**, 149
- Tejeda, G., Carmona-Novillo, E., Moreno, E., et al. 2015, [ApJS](#), **216**, 3
- Vissapragada, S., Buzard, C. F., Miller, K. A., et al. 2016, [ApJ](#), **832**, 31
- Wan, Y., Yang, B. H., Stancil, P. C., et al. 2018, [ApJ](#), **862**, 132
- Wind, P., & Roeggen, I. 1992, [ChPhy](#), **167**, 263
- Zarur, G., & Rabitz, H. 1974, [JChPh](#), **60**, 2057